

CHAPTER 1

Bifurcations in the Fast Dynamics of Neurons: Implications for Bursting

John Guckenheimer

*Mathematics Department, Cornell University
Ithaca, NY 14853*

Joseph H. Tien

*Center for Applied Mathematics, Cornell University
Ithaca, NY 14853*

Allan R. Willms

*Department of Mathematics and Statistics, University of Guelph
Guelph, ON, Canada N1G 2W1*

1. Introduction

Models of neuronal bursting have been studied extensively as illustrated throughout this volume. Different types of periodic bursting have been observed and classified according to criteria related to bifurcation theory^{25,3,19}. From the perspective of (geometric) singular perturbation theory²⁰, bursting is viewed within the context of systems with multiple time scales – normally a slow time scale and a fast time scale. Most work has focused upon the “slow motion” of the system during quiescent and active portions of a bursting cycle. During these epochs, the system state is described by attractors that evolve on the slow time scale. The transitions between quiescent and active states are marked by bifurcations of the “fast subsystem.” In the singular limit of an infinite separation of time scales, the slow variables of a system remain fixed on the fast time scale and become parameters in the fast subsystem. Singular perturbation theory describes how this picture applies to situations in which the time scales are well, but

not infinitely, separated. The separation of time scales is not always apparent in the equations themselves, so we seek computational methods that perform slow-fast decompositions of the dynamics.

The focus of this paper is upon the bifurcation analysis of the fast subsystems of neuronal models of bursting. Because these bifurcations mark the transitions between active and quiescent states in bursting rhythms of model neurons, they play a key role in determining which types of bursting can occur in the model. The hypothesis we explore in this paper is that there are widespread similarities among the fast subsystems of many models. The basis for this hypothesis is that spike generating sodium currents are often the largest and fastest currents in neurons, consequently representing a central part of the fast subsystem. Moreover, less variability has been found in fast sodium channels than in other common types of channels¹⁷. This prompts us to study a model with only a fast sodium current and a passive leak conductance. Using the Hodgkin-Huxley representation of the sodium conductance and making the familiar assumption that the activation of this current is “instantaneous” yields a two dimensional vector field. The bifurcations of this model can be studied thoroughly, although the numerical analysis must confront issues arising from multiple time scales. These issues were already apparent in early work of Fitzhugh¹¹. His work depicts a “no man’s land” in the phase space of a reduced Hodgkin-Huxley model that foreshadows numerical issues in determining the bifurcation diagrams of these systems. The “cusp and loop” structure for bifurcations of equilibrium points in this model form a paradigm for the bifurcations of many neural models.

Classifications of bursting oscillations have not yet produced a good understanding of how to “tune” models to produce different types of oscillations. Parameter space maps¹³ obtained from bifurcation analysis and/or systematic variation of parameters in neural models display how parameters such as maximal conductances of different channels interact to produce different oscillatory rhythms. Numerical computations answer questions about the types of bursting for any chosen set of parameter values without yielding a clear intuition of what will happen in a new model or in different parameter ranges. By investigating how our analysis applies to several bursting models, we take a step here towards the development of predictive guidelines describing which characteristics of a model lead to different kinds of bursting.

2. A Two Dimensional Model of Spiking sodium currents

In this section, we study the following two dimensional vector field:

$$\begin{aligned}
 \dot{v} &= -(g_{Na}m^3h(v - v_{Na}) + g_l(v - v_l)) \\
 \dot{h} &= \alpha_h(v)(1 - h) - \beta_h(v)h \\
 \alpha_h(v) &= 0.07 \exp\left(\frac{-60 - v}{20}\right) \\
 \beta_h(v) &= \frac{1}{1 + \exp\left(\frac{-30 - v}{10}\right)} \\
 m &= \frac{1}{1 + \exp\left(\frac{-(v + 35)}{9}\right)}
 \end{aligned} \tag{1}$$

This vector field is derived from the Hodgkin-Huxley model for squid giant axon¹⁸ by

- assuming that the gating variable m is at its steady state,
- eliminating the potassium current,
- replacing the steady state curve of m by a sigmoidal “Boltzmann” that is a good approximation to the Hodgkin-Huxley representation but analytically simpler, and
- assuming that the capacitance and temperature dependent parameters in the model are both 1

We shall set $g_{Na} = 120$, the value used by Hodgkin-Huxley, in these equations.

We regard this as a minimal model for action potentials, representative of the fast dynamics of more complex model neurons containing additional conductances. In such models, if the gating of other conductances is sufficiently slow, then we examine the singular limit in which they are constant. The sum of these currents then has the form of a “leak” conductance, the term $g_l(v - v_l)$ in equation (1) for \dot{v} . Modulation of the slow currents or changes in their values on slow time scales can be represented as variations of these parameters. Thus, crossing bifurcation boundaries in the model is correlated with changes in the firing properties of the neuron. This is the conceptual basis for the multiple time scale analysis of neuronal bursting. Our primary interest in this section is to investigate how the dynamics of system (1) depend on the parameters g_l and v_l . The two parameter bifurcation diagram of system (1) yields predictions about the types of transitions that could occur at the initiation or termination of a burst of action potentials in neurons for which the sodium current is the dominant fast current.

We analyze several bursting model neurons in Section §3 from this perspective.

The bifurcation theory of two parameter families of two dimensional vector fields has been thoroughly studied²⁸. We employ the classification of codimension one and two bifurcations in generic families of planar vector fields to describe the bifurcation diagram of (1). This turns out to be a more difficult enterprise than initially might be expected, due to the fact that system (1) itself has two time scales. The insights of geometric singular perturbation theory point to phenomena that occur on tiny length scales in parameter space, making it difficult to numerically resolve some aspects of the bifurcation diagram. In particular, we find thin parameter regions in which periodic orbits contain “canards,” segments that track unstable slow manifolds of the system in Fitzhugh’s no man’s land. Some bifurcation curves lie very close together in these regions.

There are four types of codimension one bifurcations in planar vector fields with at most one saddle point:

- (1) Hopf bifurcation - an equilibrium has Jacobian with trace 0 and positive determinant
- (2) Saddle-node bifurcation - an equilibrium has Jacobian with 0 determinant
- (3) Homoclinic bifurcation - a stable and unstable separatrix of a saddle point coincide
- (4) Saddle-node bifurcation of a periodic orbit - the return map of the periodic orbit has derivative 1 at its fixed point

Normal forms and unfoldings of these bifurcations characterize the types of qualitative changes occurring in the phase portraits near the bifurcations¹⁴. There are several different types of codimension two bifurcations that occur in this system. We introduce them as they are encountered in our description of the bifurcation diagram.

Figure 1 shows a numerically computed bifurcation diagram in the (g_l, v_l) parameter plane. The curves of saddle-node bifurcations drawn as solid curves and Hopf bifurcations drawn as dashed curves were computed explicitly with the symbolic computer package Maple. Writing $J(v, h, g_l, v_l)$ for the Jacobian of the vector field, the defining equations for Hopf bifurcation are $\dot{v} = \dot{h} = \text{tr}(J) = 0$ and the defining equations for saddle-node bifurcations are $\dot{v} = \dot{h} = \text{det}(J) = 0$. These equations depend upon v in a complicated manner, but their dependence upon h and the parameters is simpler. Therefore, we make v the continuation parameter in our cal-

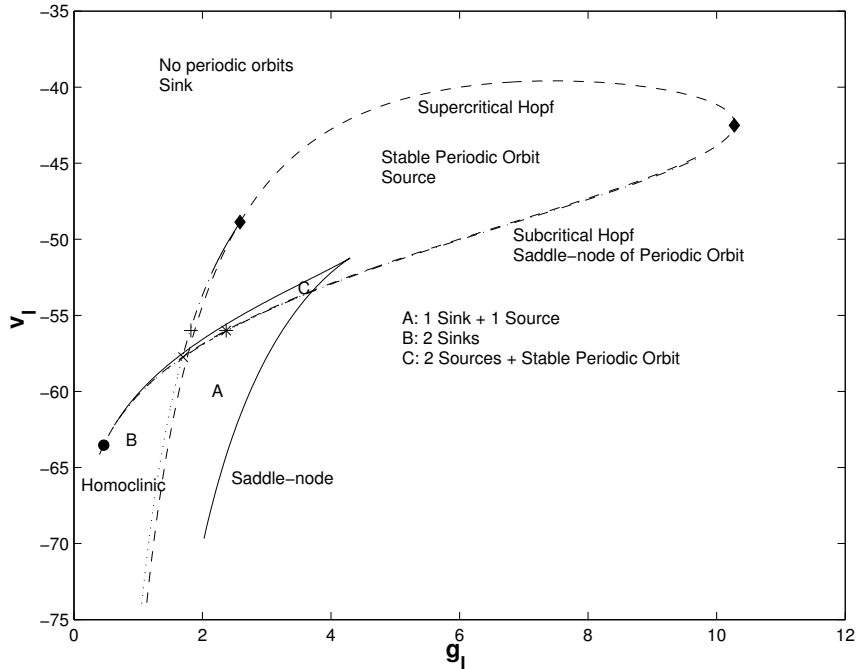


Fig. 1. Bifurcation diagram of the system (1) in the (g_l, v_l) plane of parameters. Saddle-node bifurcations are shown as a solid curve, Hopf bifurcations as a dashed curve, saddle-node of periodic orbit bifurcations as dash-dotted curves and homoclinic bifurcations as dotted curves. The two degenerate Hopf bifurcations are marked with diamonds and the Takens-Bogdanov point with a filled circle. The plus, cross and asterisk mark parameter values for which the phase portraits are displayed below.

culations. This means that we obtain h, g_l, v_l as functions of v along each bifurcation curve. This is done as follows. The equation $\dot{h} = 0$ is independent of the parameters and linear in h , so we solve $\dot{h} = 0$ first to obtain h as a function of v at equilibrium points. This value of h is substituted into the other equations. Next, we observe that $\text{tr}(J) = 0$ and $\det(J) = 0$ are independent of v_l and depend linearly on g_l , so $\text{tr}(J) = 0$ is solved for g_l in the case of Hopf bifurcation, and $\det(J) = 0$ is solved for g_l in the case of saddle-node bifurcation. Finally, when the values of g_l and h are substituted into the equation $\dot{v} = 0$, we obtain a linear equation for v_l that is then solved. Solving these successive equations gives (h, g_l, v_l) as functions of v along the saddle-node and Hopf bifurcation curves. The expressions are lengthy, but Maple performs the calculation readily.

The number of equilibrium points of the system changes from one to three upon crossing the saddle-node curve¹⁴. This curve has a codimension two cusp bifurcation¹⁴ located near $(g_l, v_l) = (4.29367, -51.2428)$. The “interior” of the cusp is the region in which there are three equilibria. When there are three equilibria, exactly one of the three is a saddle. There is a second codimension two bifurcation point, called a Takens-Bogdanov bifurcation¹⁴, near $(g_l, v_l) = (0.46387, -63.5318)$. The Takens-Bogdanov bifurcation is located by a filled circle in Figure 1. The saddle-node and Hopf curves intersect tangentially at the Takens-Bogdanov point, and the Hopf curve terminates because $\det(J)$ changes sign on the curve defined by $\dot{v} = \dot{h} = \text{tr}(J) = 0$ at this point. Theoretical analysis¹⁴ demonstrates that there is also a curve of homoclinic bifurcations that terminates at the Takens-Bogdanov point.

Periodic orbits emerge from equilibrium points undergoing Hopf bifurcation¹⁴. There is a “Lyapunov” quantity determined by the third degree Taylor expansion of the vector field at each Hopf bifurcation point which determines the stability of the orbits. The Lyapunov quantity of supercritical Hopf bifurcations is negative and the periodic orbits are stable. At subcritical Hopf bifurcations the Lyapunov quantity is positive and the periodic orbits are unstable. In the system (1), there are a pair of codimension two bifurcation points called degenerate Hopf bifurcations, where the Lyapunov quantity is zero. These two points, shown with filled diamonds in Figure 1, bound a segment of supercritical Hopf bifurcations, with the remainder of the Hopf bifurcation curve consisting of subcritical bifurcations. The Hopf curve also has a point of self-intersection where the two equilibrium points that are not saddles simultaneously undergo subcritical Hopf bifurcation.

The properties of a structurally stable planar vector field are characterized by its equilibrium points and their stability, its periodic orbits and their stability, and by the limit sets of saddle separatrices. Thus we want to locate periodic orbits and saddle separatrices and see how they change as the parameters (g_l, v_l) vary. We have pointed out that periodic orbits emerge at Hopf bifurcations. Families of periodic orbits in planar vector fields can also terminate in three other ways.

- (1) At saddle-nodes (also called folds) of periodic orbits, a stable periodic orbit and an unstable periodic orbit coalesce into a single orbit that is stable from one side and unstable from another.
- (2) At homoclinic bifurcations a family of periodic orbits terminates as it approaches a saddle point and its period grows without bound.

- (3) A periodic orbit may approach a saddle-node equilibrium point at a saddle-node bifurcation of a parameter. The equilibrium emerges “astride” the periodic orbit, and once again the period of the periodic orbit grows unbounded as the bifurcation is approached. Rinzel and Ermentrout²⁶ call these bifurcations saddle-nodes in cycles (SNIC).

We seek to compute the bifurcation curves for saddle-nodes of periodic orbits and homoclinic bifurcations. Homoclinic orbits can only exist when there is a saddle equilibrium; i.e., inside the cusp. We used a “shooting” strategy to compute parameter values for homoclinic bifurcations. The defining equation for homoclinic bifurcation can be expressed in terms of a cross-section Γ to the homoclinic orbit. As a parameter is varied, the intersections of the stable and unstable manifolds of the saddle with Γ smoothly switch sides, coinciding at the bifurcation value of the parameter. In terms of a coordinate along Γ , the difference between the intersection of the stable and unstable manifolds of the saddle with Γ is a defining function for the homoclinic bifurcation. We begin with parameter values that straddle the bifurcation and employ a secant method to converge to a bifurcation value. A bisection algorithm could also be used. Beginning with two nearby points on a curve of homoclinic bifurcations, a simple extrapolation procedure is used to search for new starting parameter values that straddle the bifurcation curve. This procedure readily detects two intersecting curves of homoclinic bifurcations in which the interior of the homoclinic orbit makes a convex angle at the saddle point. In addition to these “small” homoclinic orbits, there are two families of “large” homoclinic orbits in which the angle made by the interior of the homoclinic orbits is larger than π . In generic families, the two bifurcation curves of large homoclinic orbits terminate at the intersection of the bifurcation curves of small homoclinic orbits. This intersection is a codimension two “gluing bifurcation” where the stable and unstable manifolds of the saddle form a figure eight¹². The large homoclinic orbits closely follow branches of small homoclinic bifurcation.^a If one varies parameters and solves the initial value problem, it can be difficult or impossible to locate parameter values in the very narrow strip between the large and small bifurcation curves.

^aTo reliably compute the large homoclinic bifurcations with a shooting algorithm, it is important to choose a cross-section for which the intersections with the appropriate branches of the stable and unstable manifolds of the saddle vary smoothly in a substantial neighborhood of the bifurcation.

Figure 2 is a qualitative depiction of the region around the gluing bifurcation in Figure 1. This is one region in which we need to rely upon theoretical insight to develop a consistent bifurcation diagram. The figure shows the relative position of the large and small homoclinic bifurcation curves as well as the location of the curve of saddle-node of periodic orbit bifurcations discussed below. At each homoclinic bifurcation curve, there is one family of periodic orbits that terminates. Periodic orbits that surround the right hand equilibrium point (i.e. the equilibrium with larger h) exist in the strip between the Hopf bifurcation of the right-hand equilibrium and the curve of small homoclinic bifurcations for loops that surround this equilibrium. Similarly, periodic orbits surrounding the left-hand equilibrium occur in a strip between the Hopf bifurcations of this equilibrium and a small homoclinic curve. Unstable periodic orbits appear to the left and below the two curves of large homoclinic bifurcations. Figures 4, 5 and 6 lie in the region to the right of the left Hopf curve. Figure 4 lies in the region labelled with *1 between the right Hopf and the right homoclinic curve, Figure 5 lies in the region labelled with *2 between the right homoclinic curve and the large homoclinic curve, and Figure 6 lies in the region labelled with *3 below the curve of saddle-nodes of periodic orbits. The strip between the large homoclinic curve and the saddle-node of periodic orbits curve is so thin that we were unable to locate parameter values inside it.

Computation of approximate parameter values for saddle-node (or fold) bifurcations of periodic orbits in the system (1) is easier than locating the orbits themselves. At these bifurcations, there is a periodic orbit that is (weakly) stable from one side and (weakly) unstable from the other. Expressed in terms of a return map θ , the defining equations are $\theta(x) = x$ and $\theta'(x) = 1$ where x is constrained to the cross-section. However, it is difficult to compute the return map close to the bifurcating periodic orbit because one segment of the periodic orbit is highly stable and another segment is highly unstable. We discuss this behavior below in relation to the phase portrait shown in Figure 5. Therefore, we use indirect methods to locate the saddle-node of periodic orbit bifurcations. To one side of the bifurcation in the parameter space, there is a pair of nearby periodic orbits, one stable and one unstable. To the other side of the bifurcation, there are no nearby periodic orbits. Outside the cusp of saddle-nodes of equilibria, we followed the curves of saddle-nodes of periodic orbits by searching for the boundary between parameter regions with and without periodic orbits. This procedure is time consuming, but accomplishes the desired task reasonably well. The curves extend into the interior of the cusp where they

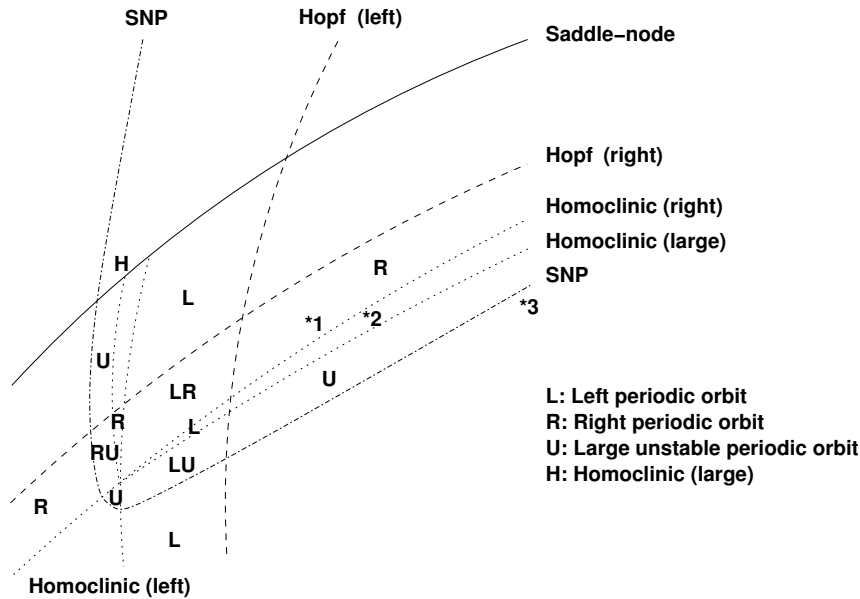


Fig. 2. Qualitative depiction of the bifurcation diagram of the system (1) near the codimension two gluing bifurcation where homoclinic curves cross. Regions are labelled with the type(s) of periodic orbits found at parameter values in the region. R and L indicate periodic orbits surrounding a single equilibrium point on the right or left in Figures 4, 5 and 6; U indicates that there is an unstable periodic orbit surrounding all three equilibria. Above and to the right of the saddle-node of periodic bifurcation curve (labelled SNP), there is also a stable periodic orbit surrounding all of the equilibrium points. The labels *1, *2 and *3 show the regions to which Figures 4, 5 and 6 belong, respectively.

lie very close to the curves of large homoclinic bifurcations. The end of each curve of saddle-node bifurcation of periodic orbits that lies outside the cusp region terminates at a degenerate Hopf bifurcation, near parameter values $(g_l, v_l) = (2.5851, -48.870), (10.277, -42.513)$. These are marked by diamonds in Figure 1.

Figures 3–7 show five phase portraits from different regions in the bifurcation diagram, illustrating varied aspects of this system. Referring to Figure 1, the locations of these parameter values are marked on this bifurcation diagram. We use the following conventions in these phase portraits: sinks are drawn as triangles, saddles as +’s and sources as squares. The stable and unstable manifolds of the saddles and the periodic curves are drawn as solid curves, while the h nullclines are drawn as dotted curves and the v nullclines are dash-dotted curves.

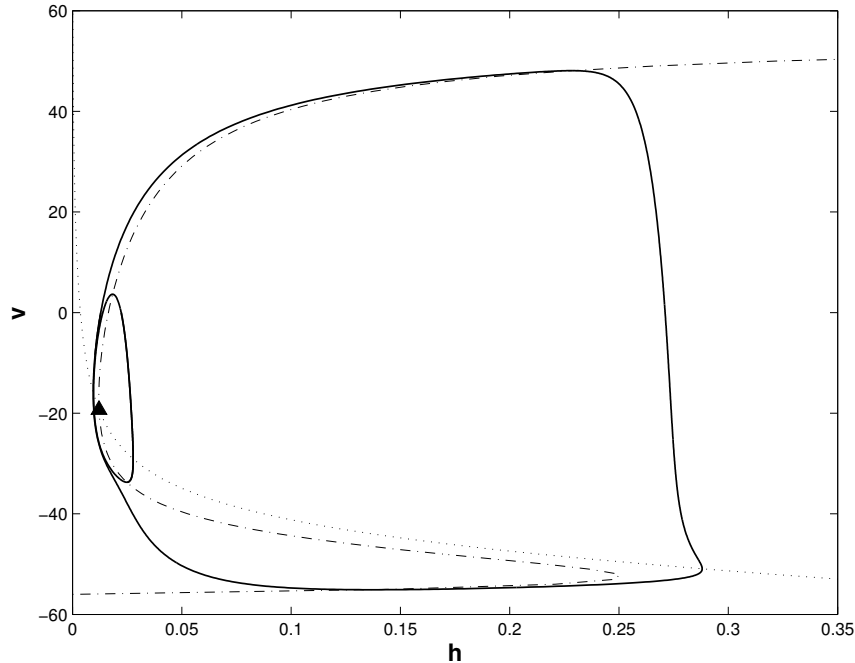


Fig. 3. Phase portrait of the system (1) for $(g_l, v_l) = (1.82, -56)$. There is a sink, unstable periodic orbit (small) and stable periodic orbit (large). Nullclines are plotted as dotted and dash-dotted curves.

Figure 3 shows a phase portrait for parameters $(g_l, v_l) = (1.82, -56)$, depicted by the + on the bifurcation diagram in Figure 1. These parameter values lie outside the cusped region bounded by the saddle-node bifurcation curve, and it lies between the Hopf curve and the curve of saddle-nodes of periodic orbits. As shown in the phase portrait, there is a stable equilibrium, a small unstable periodic orbit and a large stable periodic orbit. The unstable periodic orbit divides the basin of attractions of the equilibrium and the stable periodic orbit.

The three phase portraits in Figures 4, 5 and 6 correspond to parameter values $(2.38643, -56)$, $(2.3864443369, -56)$, and $(2.386444337, -56)$. These nearby parameter values are located at the asterisk in Figure 1. There are four bifurcation curves that pass through this region of Figure 1: from top to bottom these are a curve of Hopf bifurcations, a curve of small homoclinic orbits with loops that lie below and to the right of the saddle point, a curve of large homoclinic orbits with loops in which the upper unstable separatrix

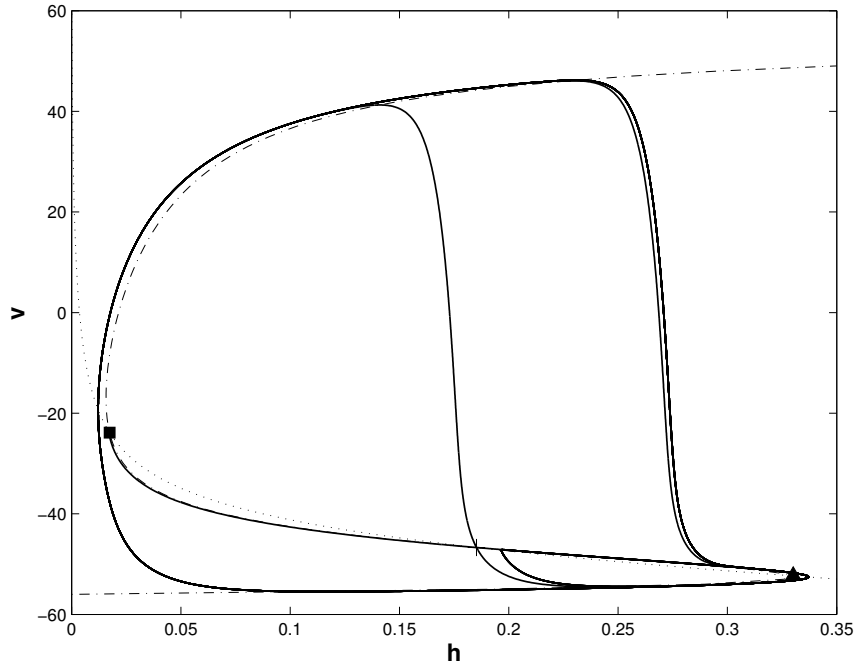


Fig. 4. Phase portrait of the system (1) for $(g_1, v_1) = (2.38643, -56)$. There is a sink (triangle), a source (square) and a saddle (+). Both separatrices of the unstable manifold of the saddle tend to a stable periodic orbit and the right separatrix of the stable manifold limits on an unstable periodic orbit. In this and the subsequent figures, the unstable manifold leaves the saddle more vertically than the stable manifold.

of the saddle returns to the saddle along the right branch of the stable manifold, and a curve of saddle-nodes of periodic orbits. The parameter values $(2.38643, -56)$ lie between the Hopf curve and the first curve of homoclinic bifurcations; the parameter values $(2.3864443369, -56)$ lie between the two homoclinic curves, and the parameter values $(2.386444337, -56)$ lie below the curve of saddle-nodes of periodic orbits. Phase portraits above the Hopf curve lie in region C of the bifurcation diagram and have two sources and a stable periodic orbit. In region C , each branch of the stable manifold of the saddle comes from a source. Figure 4 depicts a phase portrait below the Hopf curve: there is a sink, a saddle and a source. The stable manifold of the saddle has one separatrix that comes from the source, while the other comes from an unstable periodic orbit that bifurcated from the right-hand equilibrium point at its (subcritical) Hopf bifurcation. For the parameter

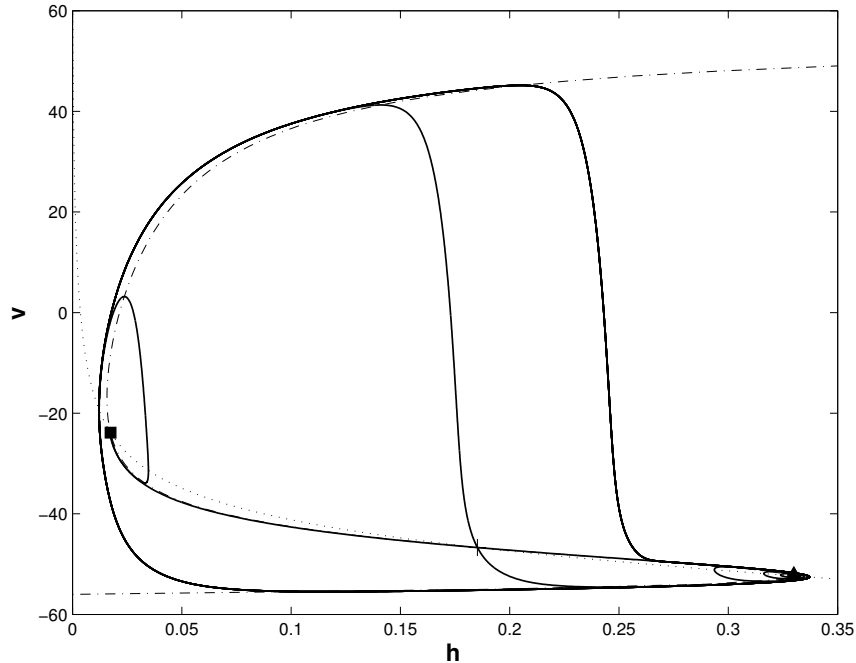


Fig. 5. Phase portrait of the system (1) for $(g_l, v_l) = (2.3864443369, -56)$. The change that has occurred from Figure 4 is that the lower separatrix of the unstable manifold of the saddle and the right separatrix of the stable manifold have crossed in a homoclinic bifurcation, annihilating the unstable periodic orbit in the process.

values shown, this periodic orbit is close to forming a homoclinic orbit with the saddle. Both branches of the unstable manifold tend to the stable periodic orbit surrounding all three equilibrium points. As one passes the first homoclinic curve between the phase portraits of Figure 4 and Figure 5, the unstable periodic orbit disappears, the lower branch of the unstable manifold of the saddle tends to the sink and right branch of the stable manifold comes from the source. As g_l increases slightly from 2.3864443369, the right branch of the stable manifold of the saddle and the upper branch of its unstable manifold coalesce into a homoclinic orbit. Crossing this homoclinic orbit generates a new unstable periodic orbit surrounding all three equilibrium points because the trace at the saddle is positive. This unstable periodic orbit quickly collides with the stable periodic orbit in a saddle-node of periodic orbits bifurcation, annihilating both. Figure 6 shows a phase portrait for parameter values just to the right of the saddle-node of

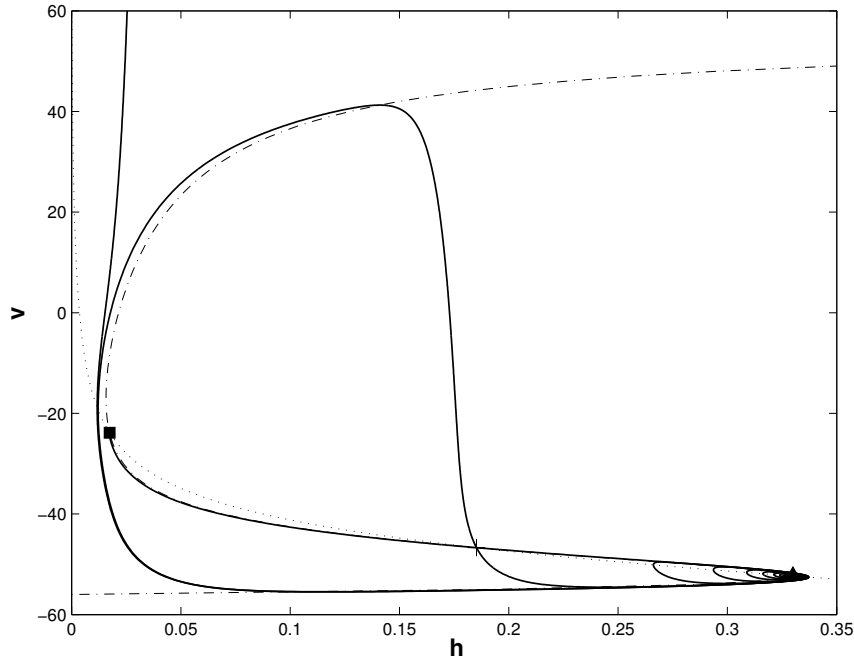


Fig. 6. Phase portrait of the system (1) for $(g_l, v_l) = (2.386444337, -56)$. The changes that have occurred from Figure 5 are that the upper separatrix of the unstable manifold of the saddle and the right separatrix of the stable manifold have crossed in a homoclinic bifurcation, recreating an unstable periodic orbit that then coalesced with the stable periodic orbit in a saddle-node of periodic orbits.

periodic orbits bifurcation. Both branches of the unstable manifold of the saddle tend to the sink in this phase portrait and no periodic orbits remain in the phase portrait.

These numerical calculations indicate that the distance between the second homoclinic bifurcation curve and the saddle-node of periodic orbits is smaller than 10^{-9} , and we have been unsuccessful in finding parameter values between these two curves. This is hardly surprising given the nature of the flow in this parameter region. The second homoclinic orbit is an example of a “canard.” This term from singular perturbation theory refers to a trajectory that follows an unstable branch of a slow manifold. We explain what this means in the context of Figure 5. Away from the v nullcline, the magnitude of \dot{v} is much larger than the magnitude of \dot{h} . Consequently, we regard v as the “fast” variable of the system and “ h ” as the slow variable. Trajectories are attracted to a neighborhood of the v nullcline where they

turn and flow slowly along this nullcline until reaching a place where the nullcline is parallel to the v axis. The typical behavior at these folds is for trajectories to “jump” to the opposite branch of the nullcline. At the right hand fold, this does not happen for the unstable manifold of the saddle in the small parameter range we are investigating. Instead, the unstable manifold tends back along the middle, unstable branch of the v nullcline. Only later does it jump. This branch of the nullcline closely approximates the stable manifold of the saddle. The eigenvalues at the saddle are approximately -0.05 and 3 , so the exponential rate of divergence away from the stable manifold is 60 times faster than the exponential rate of attraction to the saddle along the manifold. In order to approach the saddle along the stable manifold, a trajectory must be extremely close to the stable manifold. Using estimates from the linear approximation at the saddle, the distance from the stable manifold grows by a factor $2^{60} \approx 10^{18}$ as the distance from the saddle decreases by a factor of only $1/2$. Consequently, even the round-off errors of floating point arithmetic preclude integration of the unstable manifold back close to the saddle. The region near the stable manifold is Fitzhugh’s “no man’s land” – numerical integration of trajectories starting outside the region do not enter it. As the parameter g_l changes, the unstable and stable manifolds of the saddle sweep past each other. The “take off” point for where the unstable manifold diverges from the stable manifold changes so rapidly that it appears discontinuous in the numerical integrations when the manifolds cross. The second homoclinic orbit bifurcation and the saddle-node of periodic orbit bifurcation both come from trajectories containing segments inside this “no man’s land,” that bounds the apparent discontinuity. The bifurcations are too close together in parameter space to resolve without greatly extended precision for the calculations.

Finally, Figure 7 shows the phase portrait of (1) for parameter values $(g_l, v_l) = (1.7, -57.75)$, marked by the cross in Figure 1 near the intersections of the homoclinic curves. This phase portrait shows *tristability*: there are two stable equilibria and a stable periodic orbit representing tonic spiking of the system. The domains of attraction of the stable equilibria are bounded by unstable periodic orbits that emerged from the equilibria at subcritical Hopf bifurcations. Note that the parameter values are also close to the self intersection of the Hopf curve in Figure 1. At the codimension two gluing bifurcation, both of the unstable periodic orbits grow to homoclinic orbits. The stable and unstable manifolds of the saddle point form a figure eight at the gluing bifurcation. In the parameter space, all of the homoclinic bifurcation curves meet at this gluing bifurcation.

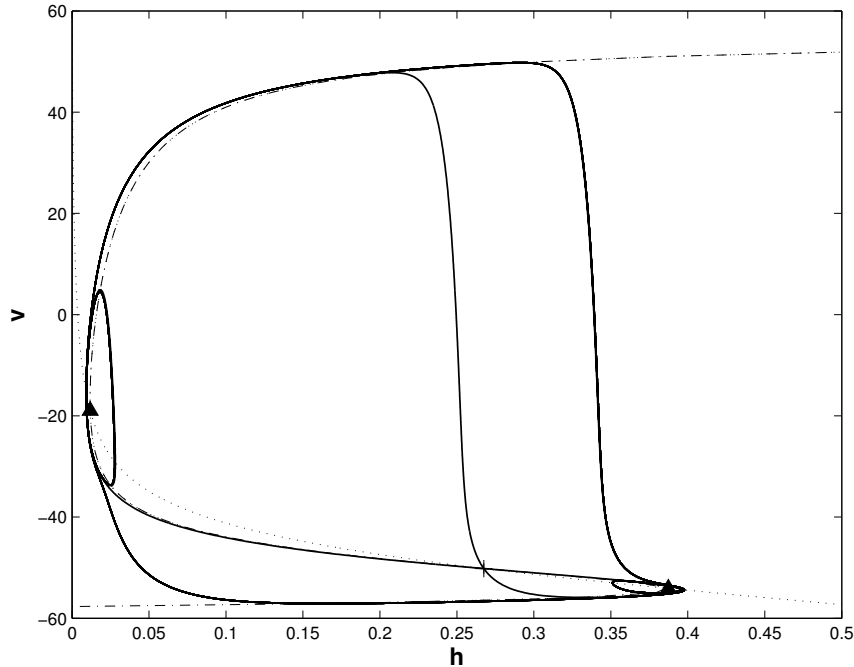


Fig. 7. Phase portrait of the system (1) for $(g_l, v_l) = (1.7, -57.75)$. There are two sinks (triangles), a saddle, a stable periodic orbit and two unstable periodic orbits. The system is tristable with three attractors.

We note that the global homoclinic and saddle-node of periodic orbit bifurcation curves in Figure 1 lie close to the steady state Hopf bifurcation curves. This property of the system can be attributed to the stiffness of system (1) in which v is a fast variable relative to h . Hopf bifurcation in a two dimensional fast-slow system occurs when equilibrium points lie close to a fold of the slow manifold. As analyzed by Dumortier and Roussarie⁹ and others^{1,10}, the periodic orbits growing from these bifurcation acquire canards and pass through a parameter regime in which their size changes extremely rapidly. Global bifurcations are likely to be found, as they are here, in the canard regions. In the next section, we analyze models of bursting neurons and encounter higher dimensional fast subsystems than the one described in this section. Although we do not show the global bifurcations of these models, we expect, and preliminary calculations confirm, that many will be found close to curves of equilibrium point bifurcation as is the case in this model.

3. Fast-slow Analysis of Bursting

Bursting in neuronal models refers to compound oscillations which have an “active” phase consisting of action potentials and a quiescent phase without action potentials during each period of oscillation. Geometric singular perturbation theory interprets the transitions between active and quiescent phases as bifurcations in a fast subsystem of the model, occurring as the parameters of the fast subsystem change on the slow time scale. We investigate when the results of the previous section can be applied directly to models of bursting, assuming that time constants of gating variables for other currents are slower than the inactivation time scales of the sodium current. Although this requirement is seldom satisfied (even in the original Hodgkin-Huxley model), this analysis gives insight into the role that additional currents play in the initiation or termination of action potentials.

This section examines these ideas within the context of several models of neuronal bursting. We approach the separation of fast and slow components of a system in different ways. Most of the mathematical theory is formulated in terms of systems in which some phase space variables are slow and others are fast. This is made explicit by a small parameter ε that is the ratio of time scales, and ε approaching 0 gives a singular limit in which the slow variables no longer change on the fast time scale. Here we take a somewhat different approach based upon the representation of transmembrane current as a sum of currents associated with different channels. We separate currents into ones we regard as fast and ones we regard as slow because this allows us to map the slow dynamics of the system into variations of the leak parameters in the fast subsystem. However, the phase space variables are gating variables of the currents and currents with fast activation and slow inactivation are not readily assigned to the slow or fast categories.

The currents in all the models that we investigate have the Hodgkin-Huxley representation

$$I_y = g_y m_y^p h_y (V - V_y),$$

where g_y is a constant conductance, V_y is the reversal potential, p is a positive integer, and m_y and h_y are activation/inactivation variables or functions that take values in the range $[0, 1]$. Non-inactivating currents can be written in this form with h_y set to be identically equal to 1; a passive leak current has both m_y and h_y set identically to 1. The voltage equation

in these models may be then written as

$$C_m \frac{dV}{dt} = - \sum_y I_y,$$

where C_m is the membrane capacitance. We do not consider directly the effects of an “injected” current in these neuronal models, but this can be investigated indirectly as a change in the reversal potential of a leak conductance. Our strategy is to map the slow currents into an “effective” leak current of the fast subsystem, regarding the reversal potential and conductance of this leak current as slowly varying variables. Specifically, we define the effective leak parameters as

$$g_{L\text{eff}} = \sum_y g_y m_y^p h_y$$

$$V_{L\text{eff}} = \left(\sum_y g_y m_y^p h_y V_y \right) / g_{L\text{eff}}$$

the sum being taken over the slow currents. The ranges of the activation/inactivation functions yield a region in the $(g_{L\text{eff}}, V_{L\text{eff}})$ -plane inside which the effective leak parameters are confined.

Analysis of bifurcations of the fast subsystems as the effective leak conductance and reversal potential are varied must be repeated for each model. Methods like those described in the previous section readily yield the bifurcation curves for saddle-node and Hopf bifurcations of equilibria. When the dimension of a fast subsystem is larger than two, computation of the global bifurcations are problematic for two reasons. First, the methods for computing these curves in multiple time scale systems discussed in the previous section were specific to planar vector fields, and robust algorithms that address these numerical issues in the context of higher dimensional vector fields are not as well developed. Second, more complicated limit sets can and do occur, even in the context of the original Hodgkin-Huxley model for squid axon¹⁵. Consequently, we show only the equilibrium point bifurcation curves in the examples discussed below.

3.1. *Aplysia*

The R15 neuron of *Aplysia* is a bursting neuron whose electrophysiology has been studied by many researchers, e.g.^{21,4}. One of the simplest models of bursting in this neuron is given by Rinzel and Lee²⁷, which is based on a model by Plant²⁴. Their model involves a sodium current I_{Na} with

instantaneous activation; a potassium current, I_K ; a passive leak current, I_L ; a slow calcium current, I_{Ca} ; and a calcium-activated potassium current, I_{K-Ca} . Their work is a paradigm for the application of singular perturbation methods to analyze bursting. They chose fast subsystem variables to be the membrane potential, the sodium inactivation gating variable, and the potassium activation gating variable. The activation of the calcium current and the intra-cellular calcium concentration constitute the slow subsystem, giving a five dimensional phase space.

Here we regard the calcium and calcium-activated potassium currents as slow, and the sodium and potassium currents as part of the fast subsystem. We combine the calcium, calcium-activated potassium currents and leak currents of the full model to obtain the effective leak parameters of the fast subsystem. The region in the (g_L, V_L) plane in which the effective leak parameters are confined is shown in gray in Figure 8B and D.

Figure 8A shows a typical bursting trajectory from which we calculate the effective leak parameters for a bursting cycle. These effective leak parameters are plotted in Figure 8B along with the bifurcation curves. Figure 8C shows a plot of V vs. g_{Leff} and Figure 8D is a magnified view of the region in the (g_{Leff}, V_{Leff}) -plane where the burst cycle terminates.

Rinzel and Lee described the bursting mechanism in their model as parabolic. The bursts are apparently terminated by homoclinic bifurcations that lie close to the curve of saddle-nodes in Figure 8B. The separation between these curves is smaller than 0.1 mV in the region where the bursting stops. Note that the burst does not cease when the $(g_{Leff}-V_{Leff})$ -trajectory first crosses the bifurcation curves, but rather the trajectory crosses and re-crosses these curves several times during the last few spikes. Although the time scales of the slow currents are more than a factor of two separated from the fast currents, this separation is insufficient to exactly obtain the behavior dictated by the singular limit of slow currents that do not vary. This phenomenon is also apparent in the figures of Rinzel and Lee's work²⁷. We make the following additional observations about these bursting oscillations:

- during the quiet phase the system inhabits a region where the fast subsystem has a stable equilibrium
- slowly the effective leak reversal potential increases due to (i) reduction of Ca^{++} (which reduces I_{K-Ca} and the hyperpolarizing pull of V_K) and (ii) slow increase of I_{Ca} activation (which increases the depolarizing pull of V_{Ca})

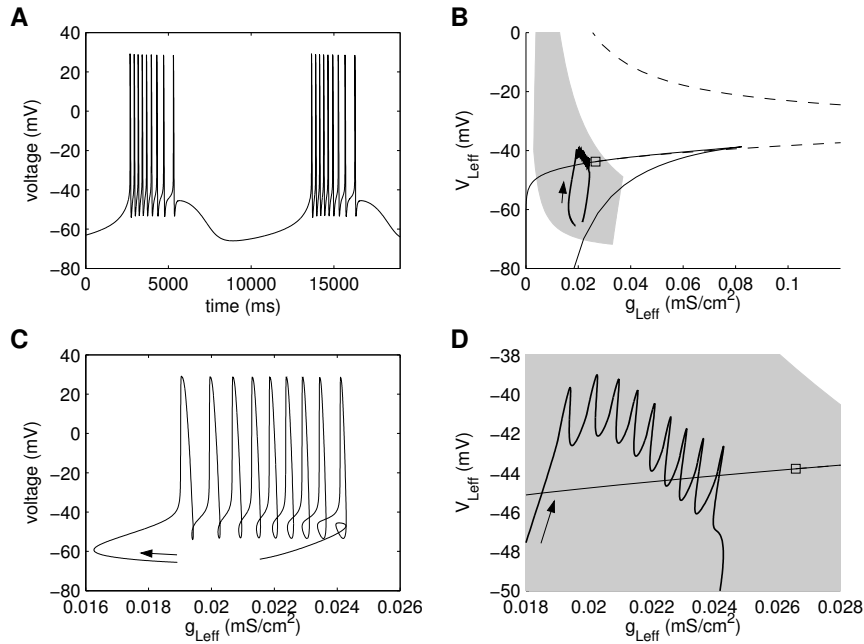


Fig. 8. Mapping of the Rinzel-Lee model to leak parameters of its fast subsystem. A: The full model's bursting trajectory. B: The effective leak parameters and equilibrium bifurcation curves. The envelope of possible leak parameters is shaded gray. The saddle-node curve is a solid line, and the Hopf curve is a dashed line that originates at a Takens-Bogdanov bifurcation (square) and extends to the right out of the panel and then passes through the panel once more on the upper right. The image of the bursting trajectory (thick solid line) lies to the left of the Takens-Bogdanov point and passes through the saddle-node curve. Arrows indicate the direction of traversal. C: Voltage vs. effective leak conductance for the burst cycle. D: Close up of B showing the region where bursting terminates.

- eventually, as $V_{L\text{eff}}$ increases, the stable equilibrium disappears in a saddle-node bifurcation and the system is immediately attracted to a periodic orbit that was born in a homoclinic bifurcation
- Figure 8B and C show that V rapidly increases with virtually no change in $g_{L\text{eff}}$ and $V_{L\text{eff}}$
- the spiking eventually stops as Ca^{++} slowly increases during the spiking, yielding a slow decrease in $V_{L\text{eff}}$ (due to the calcium-activated potassium current) that causes the trajectory to once again cross the saddle-node curve and the nearby curve of homoclinic bifurcations (Figure 8D)

- following termination of the burst, the trajectory jumps to the stable voltage equilibrium to start the cycle once again.

Thus the saddle-node and nearby homoclinic curves of the fast subsystem are of primary importance for the Rinzel-Lee bursting model.

3.2. Thalamic Relay Neurons

We next investigate a bursting model of thalamocortical relay neurons introduced by Wang²⁹. This four-dimensional model includes three fast currents: a sodium current, I_{Na} , a persistent sodium current, $I_{Na(P)}$, and a potassium current, I_K . Both sodium currents are assumed to activate instantaneously. The sodium inactivation, h , and potassium activation, n , are assumed to be related by $h = (0.85 - n)$ in accord with FitzHugh's observation¹¹. The model also includes a passive leak current, I_L , and two slow currents: a T-type calcium current, I_T , and a sag current, I_h , with reversal potential $V_h = -40$ mV. The calcium inactivation, h_T , and sag current activation, h_H , are the slow variables, although the sag current activation is rapid at high voltages so that it changes value substantially during an action potential. The calcium activation is assumed to be instantaneous. Thus I_T has a fast activation but slow inactivation, and I_h is rapid at high voltages but slow when the membrane is polarized; nonetheless, we classify both of these as slow currents. In addition, the model incorporates an injected current, which we have set at $-0.8 \mu\text{A}$; this is equivalent to a decrease in the leak reversal potential. The leak current (and injected current) along with I_T and I_h are combined to obtain the effective leak parameters of the fast subsystem.

Figure 9 shows the same information for the Wang model as Figure 8 did for the Rinzel-Lee model. The gray region in Figure 9B is a wedge where the small current I_h is responsible for the narrowness of the width, and changes in the large I_T current are responsible for movement along the length of the wedge. During the burst cycle, the effective leak parameters run along the left edge of the confining region, indicating that I_h remains very small and is not a substantial player in the bursting cycle.

Note that in comparison to the Rinzel-Lee model, where there was very little variation of $g_{L_{eff}}$ between successive spikes, Figure 9C shows that $g_{L_{eff}}$ varies substantially for the Wang model. This is a manifestation of the fact that I_T is not a completely slow current, having an instantaneous activation with a half activation value of -65 mV and saturating at about -30 mV. For this reason, the trajectory in Figure 9C has substantial horizontal move-

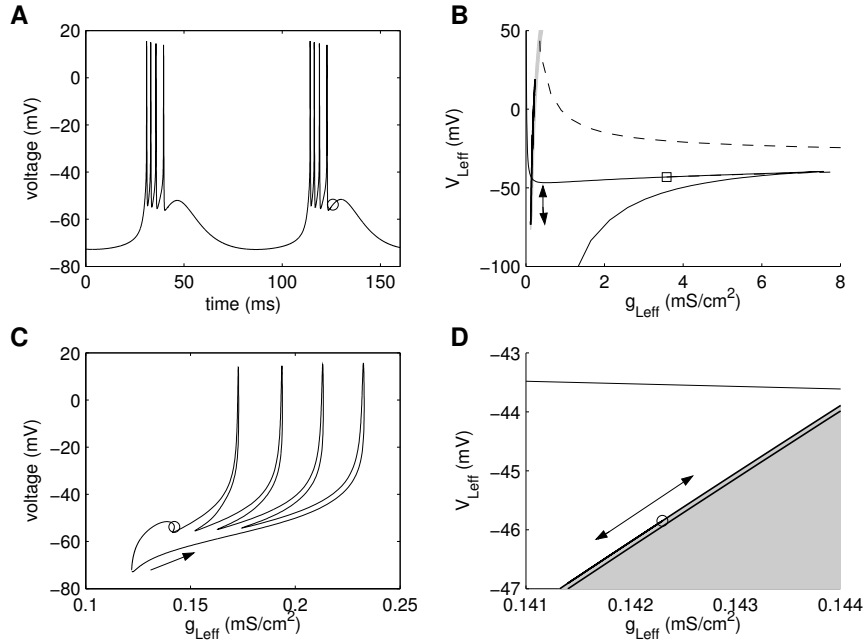


Fig. 9. Mapping of the Wang model to the two dimensional (g_{Leff}, V_{Leff}) plane. The panels of this figure parallel those of Figure 8. The circle indicates the maximum value attained by g_{Leff} and V_{Leff} after the last spike of the burst.

ment during the spikes when the voltage is below -30 mV.

In the quiescent stage of the burst cycle, the system lies near the stable equilibrium of the fast subsystem. I_T (and less importantly I_h) both slowly increase pushing the voltage upward to the spiking threshold which corresponds to the saddle-node curve of the fast subsystem where the stable equilibrium disappears. During spiking, the calcium current inactivation decreases until eventually I_T becomes too small to push the rebounding membrane above spiking threshold, thus terminating the burst. In terms of the fast subsystem, the decrease in I_T causes a decrease in V_{Leff} . Although the resolution in Figure 9B is insufficient to see this, V_{Leff} remains above the saddle-node curve during the spike train and only drops below this curve after the last spike. It then rises slightly, reaching a maximum marked by the circle in Figure 9D. Thus, as in the Rinzel-Lee model, termination of the burst cycle occurs a little below the saddle-node curve where we expect to find homoclinic bifurcations as discussed in Section 2.

3.3. Leech Heart Interneurons

Oscillations in Leech Heart Interneurons have been studied extensively by Calabrese and collaborators^{8,16,6}; a detailed model of the heartbeat elemental oscillator was constructed by Nadim et al.²² in 1995. Although the primary system here is a pair of reciprocally inhibitory neurons, they show that an individual neuron in their model can also exhibit intrinsic bursting behavior²³. This leech heartbeat model includes I_{Na} , a persistent sodium current, I_P , three different potassium currents, I_{K1} , I_{K2} , and I_A , two calcium currents, I_{CaF} and I_{CaS} , a sag current, I_h , with reversal potential -21 mV, and a passive leak current. Categorizing these currents as slow or fast is not easy. The activation and inactivation variables for some of these currents vary considerably with voltage so that the current is fast in some regimes and slow in others. For example, the activation of I_{CaS} has a time constant of about 140 ms at voltages above -40 mV, but this reduces to a fast 5 ms at voltages below -60 mV. Also a number of the currents, particularly I_{CaF} and I_{K1} , have a rapid activation but slow inactivation. In order to obtain a fast subsystem which includes all currents with fast components, we classified only I_h , I_{K2} , and I_{CaS} as slow (despite the fact that the activation for I_{CaS} is fast at hyperpolarized voltages). It should also be noted that the fast subsystem includes some components, for example the inactivations of I_{K1} and I_{CaF} , that are slower than some of the slow current components.

Figure 10 shows the same information for the leech heartbeat model as Figure 8 did for the Rinzel-Lee model. The number of spikes per burst cycle is much larger for this model than the previous ones. Spiking is initiated by a slow increase in I_h which raises the membrane potential to the point where I_{CaS} turns on and an action potential is generated. This can be seen in Figure 10D where the trajectory, starting in the lower left corner of the confining region, first moves into the region, up and to the right (I_h increasing), and then abruptly turns parallel to the left boundary of the confining region and V_{Leff} increases due to I_{CaS} turning on. After about eight spikes, g_{Leff} and V_{Leff} reach their maxima and then I_{CaS} slowly inactivates, reducing both effective leak parameters. The horizontal movement of the trajectory in the (g_{Leff}, V_{Leff}) plane is caused primarily by changes in the activation gating variable for I_{K2} which, being only moderately slow, reacts relatively quickly to changes in the membrane potential.

Termination of the burst cycle occurs shortly after I_{CaS} decreases sufficiently to cause the trajectory in the (g_{Leff}, V_{Leff}) plane to cross the saddle-

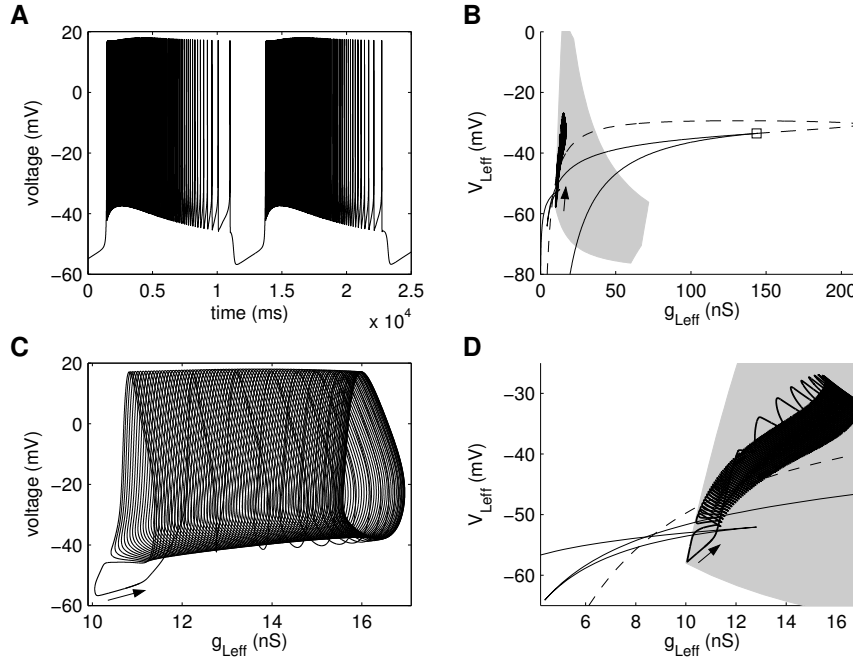


Fig. 10. Mapping of the Nadim et al. leech heartbeat model to the two dimensional $(g_{L_{\text{eff}}}, V_{L_{\text{eff}}})$ -plane. See caption to Figure 8.

node curve. Although the gross features of the saddle-node and Hopf bifurcation curves (Figure 10B) are similar in this model to the system we studied in Section 2, Figure 10D shows that the bifurcation structure for this nine-dimensional fast subsystem is more complicated at a finer scale. The saddle-node curve forms a “bow-tie” shaped region near where the hopf curve intersects it, and it is in this region that the bursting cycle is terminating.

3.4. Plateau Oscillations in Leech Heart Interneurons

Cymbalyuk and Calabrese⁷ present simpler models of leech heart interneurons than the model described above, which exhibit plateau oscillations. Their minimal model (model IV) consists of a fast sodium current, I_{Na} , a slow persistent potassium current, $I_{\text{K}2}$, and a passive leak current, I_L . Figure 11 shows the same information for this model as Figure 8 did for the Rinzel-Lee model.

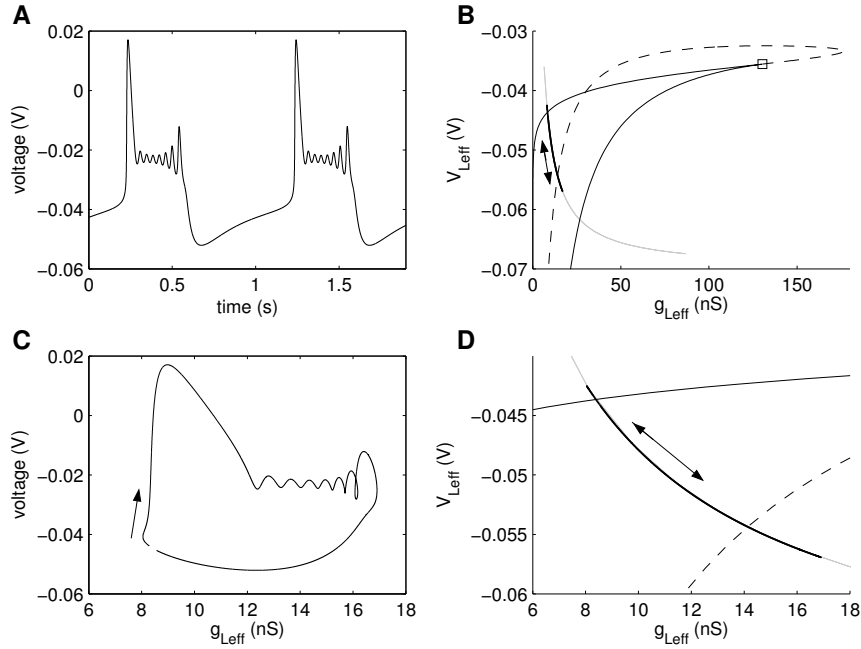


Fig. 11. Mapping of the Cymbalyuk-Calabrese simplified leech heart model to the two dimensional $(g_{L_{eff}}, V_{L_{eff}})$ -plane. See caption to Figure 8.

The shape of the saddle-node and hopf curves is similar to the “cusp and loop” structure of system (1) except that the Takens-Bogdanov point is nearly at the cusp of the saddle-node bifurcation curve. Since this model has only one slow current defined by a single activation variable, the confining region in the $(g_{L_{eff}}, V_{L_{eff}})$ -plane is a one-dimensional curve (shown in gray in Figure 11B and D). The bursting trajectory mapped to this plane traverses a portion of this curve back and forth.

During the quiescent (low voltage) phase of the burst cycle, the voltage value lies close to the low voltage fixed point in the fast subsystem, the model’s effective leak parameters lie just underneath the saddle-node curve, and I_{K2} is slowly deactivating causing a decrease in $g_{L_{eff}}$ and increase in $V_{L_{eff}}$. As $V_{L_{eff}}$ continues to increase, the system crosses the saddle-node curve, where the low voltage fixed point disappears, and the system quickly approaches the high voltage fast subsystem fixed point. This corresponds to the start of the voltage plateau. The high voltage value now activates I_{K2}

and the trajectory proceeds down and to the right in the $(g_{L_{\text{eff}}}, V_{L_{\text{eff}}})$ -plane. At about $g_{L_{\text{eff}}} = 14$, the path crosses a supercritical Hopf curve, where the high voltage fixed point becomes unstable and an attracting periodic orbit is born. This corresponds to the small amplitude plateau oscillations in Figure 11A. Eventually the attracting periodic orbit is destroyed via a saddle-node of orbits, terminating the plateau, and the system collapses to the low voltage fixed point of the fast subsystem to begin the cycle anew.

3.5. Neurons of the Pre-Bötzing Complex

Butera et al.⁵ have proposed Hodgkin-Huxley type models of neurons in the pre-Bötzing complex, a region of the brainstem essential to generating the breathing rhythm. Model I of Butera et al.⁵ consists of fast sodium and potassium currents I_{Na} and I_{K} , a persistent sodium current $I_{\text{Na(P)}}$, and a passive leak current I_L . Both sodium currents are assumed to activate instantaneously. Inactivation of I_{Na} is approximated by $1 - n$. The inactivation h of $I_{\text{Na(P)}}$ occurs on a much slower time scale than that of the other variables.

Despite the slow time scale of h , incorporating $I_{\text{Na(P)}}$ into an effective leak current does not work well here. This is partly due to the fact that, although inactivation of the persistent sodium current is slow, activation is fast. Furthermore, the true leak reversal potential and the sodium reversal potential differ significantly (approximately -60 mV for the former, +50 mV for the latter). These factors combine to result in large values of $\frac{dV_{L_{\text{eff}}}}{dt}$ during each spike.

Instead, we follow the more traditional analysis of Rinzel and Lee²⁷, and treat h as the slow variable. Figure 12 shows a burst trajectory, together with fixed points of the fast subsystem. Burst initiation corresponds to the fast subsystem passing through a saddle-node bifurcation. Burst termination occurs when the fast subsystem goes through a homoclinic bifurcation.

In addition to the leak conductance and reversal potential that we have been examining throughout this paper, we can also include the slow variable h and examine the bifurcations in the fast subsystem which result as these three parameters are varied. Note that the leak conductance and reversal potential here correspond to the true leak current in model I of Butera et al.⁵, not to an effective leak current. Figures 13(a) and (b) show the resulting hopf and saddle-node bifurcation surfaces. The shape of the hopf surface changes significantly as h is varied. On the other hand, the surface of saddle-nodes does not change much with h . Figures 13(c) and (d) show

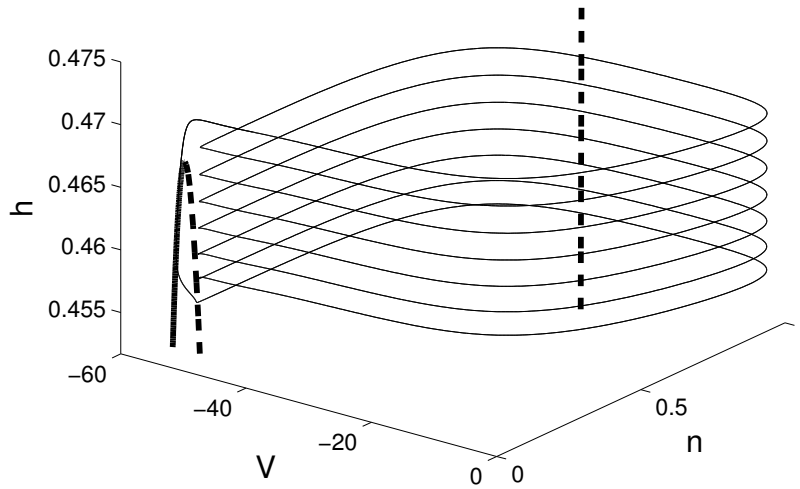


Fig. 12. A burst trajectory for Model I of Butera et al., together with fixed points of the fast subsystem. Membrane potential V and potassium activation n are the fast variables, and inactivation of persistent sodium current h the slow variable. Equilibrium points of the fast subsystem for different values of h are plotted as bold curves. Stable equilibria are plotted as the solid curve, unstable equilibria are plotted as dashed curves.

the $g_L - V_L$ bifurcation diagrams for $h = 0.21$ and $h = 0.95$, respectively. Note that Figure 13(c) resembles the bifurcation diagrams for the Rinzel-Lee, Wang, and Cymbalyuk-Calabrese models, while Figure 13(d) is similar to the bifurcation diagram of Nadim et al. The similarities in the shapes of the bifurcation curves for these different models suggest that a small number of qualitatively distinct bifurcation diagrams may predominate in the fast subsystems of Hodgkin-Huxley type models.

4. Discussion

Conductance based models for neurons with voltage gated currents based on the Hodgkin-Huxley formalism combine an equation for membrane potential with differential equations for the gating variables. Chemical concentrations of ligands or second messengers lead to a somewhat more general class

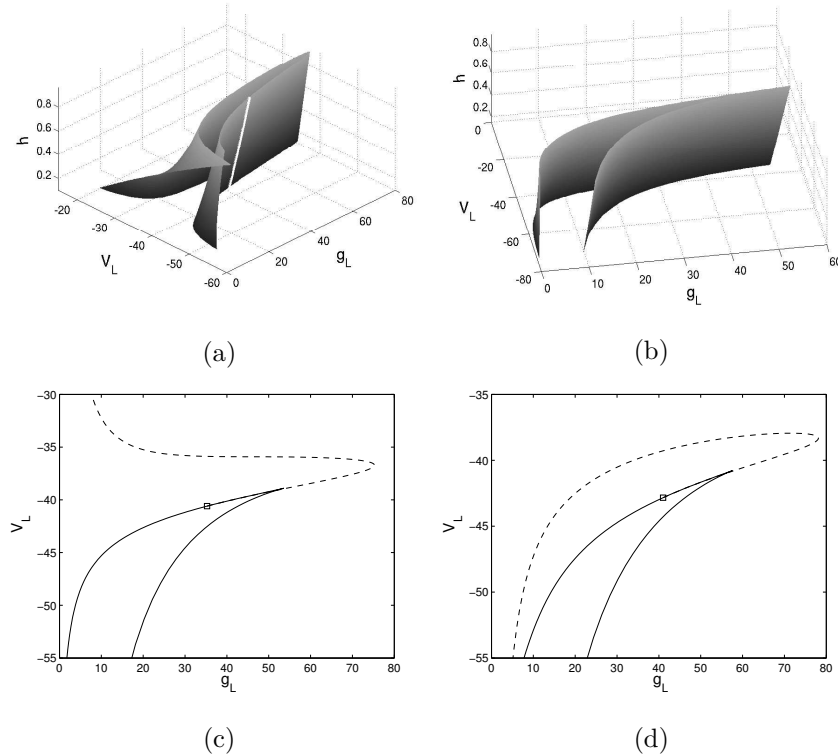


Fig. 13. Equilibrium point bifurcation diagrams of a three parameter fast subsystem (Model I of Butera et al.) with parameters (g_L, V_L, h) . (a) Hopf bifurcations, Takens-Bogdanov points, and neutral saddles. The white curve separating the two dimensional surface into two components denotes Takens-Bogdanov points. The component with larger values of V_L consists of Hopf points, while the smaller V_L component consists of neutral saddles. (b) Saddle-node bifurcations. (c) Saddle-node (solid) and Hopf (dashed) bifurcation curves in the (g_L, V_L) plane with $h = 0.21$. (d) Saddle-node and Hopf bifurcation curves in the (g_L, V_L) plane with $h = 0.95$.

of models, but the model structure is still highly constrained. We would like to determine the generality and limitations of these models in explaining observed electrical activity of neurons. Thus, we ask two complementary questions

- What types of dynamical behavior occur (generically) within this class of models?
- Are there principles that can be used to construct models and families of models that display specific types of dynamics?

The second question is often addressed in the context of fitting models to experimental data. The first question is more abstract, but even partial answers provide a framework that help us tackle the second. The questions are difficult because the dynamical behaviors we study are complex, the models have large numbers of parameters and multiple time scales bring additional challenges for the analysis. Systematically simulating models throughout biologically plausible regions of their parameter spaces is hardly feasible. Nonetheless, we speculate about generalizations in the hope that our computational and analytical studies of models will help sharpen understanding of how neural systems function.

Theories and models of bursting^{25,3,19} point to multiple time scales as a key factor in the generation of neural rhythms. We present here an analysis of neuronal bursting that makes use of three time scales. We call these time scales slow, fast and very fast. Currents that change on the slow time scale bring a neuron into and out of regimes in which it fires action potentials. The thresholds and characteristics of the action potentials are determined by dynamics of the fast and very fast time scales. The bifurcations that occur in the subsystems that incorporate the fast and very fast dynamics are shaped by the separation between the fast and very fast time scales. These bifurcations are found close to parameter values at which the subsystem has degenerate slow-fast decompositions. The proximity of various bifurcation curves to one another is explained by the extreme sensitivity of limit sets containing canards to parameter variations. Consequently, information about Hopf and saddle-node bifurcations of equilibria together with a picture of the slow manifolds in these subsystems can be used to predict information about global bifurcations. As an example, inside the cusp region of the planar vector field studied in Section §2, all the periodic orbits undergoing saddle-node bifurcations contain canards. These bifurcations lie extremely close to homoclinic bifurcations and very close to Hopf bifurcations.

We observe that the very fast subsystems of large classes of neural models are very similar to one another, describing changes in membrane potential and the rapid activation of certain currents. Typically, these activations are treated as instantaneous, removing them from the dynamical variables of the model and leaving only the membrane potential as a very fast variable. This perspective suggests that there are similarities in the bifurcation mechanisms among large classes of conductance based models for neurons. Due to their stiffness, the bifurcation diagrams of these models are difficult to determine completely, but the equilibrium point bifurcations that

are easy to determine provide a backbone on which to base further study. Section §2 presents an analysis of one such model that contains only a fast sodium and a leak current. Reductions of the Hodgkin-Huxley model embody a frequent modification of this model by including a non-inactivating potassium current whose activation is correlated with the inactivation of the sodium current. The first equation in system (1) is replaced by

$$\dot{v} = -(g_{Na}m^3h(v - v_{Na}) + g_Kn^4(v - v_K) + g_l(v - v_l))$$

with $n = h_m - h$, where h_m is often taken in the range $[0.85, 1]$. By treating g_K as a secondary parameter, we obtain a one parameter family of bifurcation diagrams. There are two notable changes in these bifurcation diagrams:

- The cusp region of saddle-nodes moves to smaller values of g_l , exiting the region where $g_l > 0$ for modest values of g_K .
- The Hopf curve undergoes a transition in which the self intersection point disappears and the curve extends upward along the positive v_l axis.

Figure 14 illustrates these changes, displaying the equilibrium point bifurcation diagram of this system with $g_K = 3$ and $h_m = 1$. These changes in the equilibrium point bifurcation structure are also associated with changes in the global bifurcation structure (saddle-nodes of orbits and homoclinics). In particular, there is no longer a crossing of the two small homoclinic curves and consequently no gluing bifurcation. Further, stable periodic orbits persist at high v_l values all the way to $g_l = 0$. Nonetheless, the curves of large homoclinic bifurcations and saddle-nodes of orbits still appear to be located extremely close to the equilibrium saddle-node curve, so that this curve remains a good indicator of where bursting will terminate.

The examples described in Section §3 illustrate two approaches to the slow-fast decomposition of neuronal models, each with advantages and disadvantages. Our results demonstrate that the equilibrium point bifurcations of a fast subsystem provide a guide to locating the transitions between spiking and quiescent dynamics in bursting rhythms. As we observe and others before us have demonstrated, some transitions between spiking and quiescent dynamics are associated with global bifurcations. However, we observe that these global bifurcations are often located close to equilibrium point bifurcations due to multiple time scales within the fast subsystems. Since the theoretical foundations for the analysis of bursting assume a large separation between slow and fast time scales, we do not expect to obtain definitive

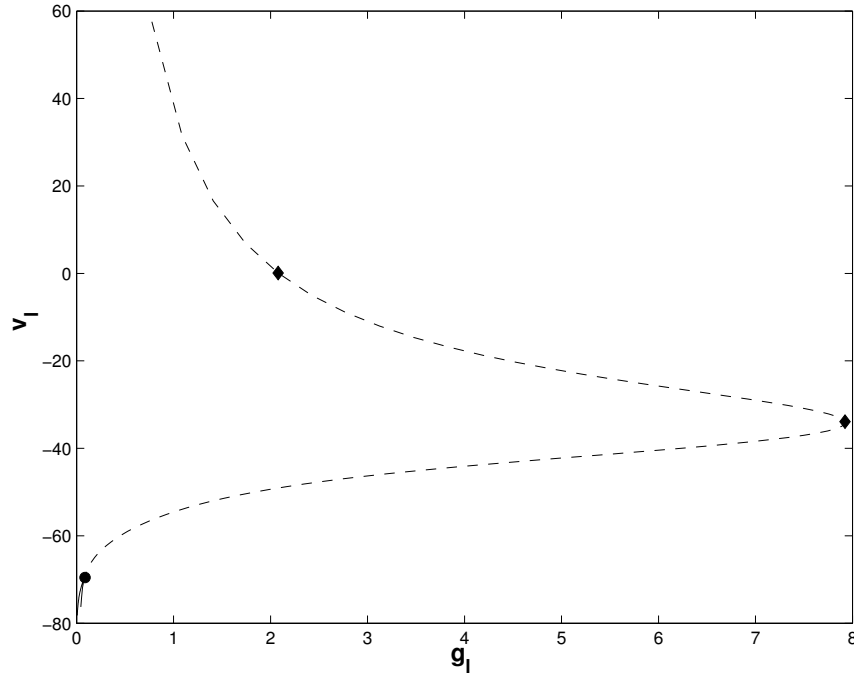


Fig. 14. The equilibrium point bifurcation diagram for the modified system (1). The conductance of the potassium current is $g_K = 3$ and $h_m = 1$. Degenerate Hopf bifurcations that bound a segment of supercritical Hopf bifurcation are marked by diamonds. The Takens-Bogdanov bifurcation is marked by a filled circle.

results about models in which these time scales blur into one another. Even so, multiple time scale analysis provides useful insight into the dynamics of these complex systems. Moreover, computational methods based upon geometric singular perturbation theory can be further refined to give still more useful insights.

In mapping slow currents to an effective leak current, we treat the effective leak conductance and reversal potential as new slow variables. The time scale of the effective leak reversal potential is affected not only by the activation and inactivation rates of the slow currents, but also by the slow currents' reversal potentials. Widely differing reversal potentials may result in a fast effective leak reversal potential, even if the gating variables of the included currents are all slow. The mapping to the effective leak current works best when the slow currents have similar reversal potentials.

The mapping of slow currents into an effective leak current gives additional information that can be used to determine whether bursting might be possible in a model. The figures of Section §3 contain gray regions that delineate possible values for the conductance and reversal potential of the effective leak current of the fast subsystems derived from a larger model. This region is determined solely by the slow currents. The extreme left point of this region is precisely the conductance and reversal potential of the true passive leak current. The lower boundary moving to the right of this point is determined by adding into the equations one slow current at a time (that is increasing its conductance from zero to its maximum value), in the order from the current with the lowest reversal potential to the one with the largest, until we reach the extreme right point where all slow currents have been added in. The upper boundary is computed similarly but taking the currents in the opposite order. Superposition of this gray region upon the bifurcation diagram of the fast subsystem restricts attention to bifurcations that might be accessible as transitions between attractors of the fast subsystem. Forcing a trajectory to cross these bifurcation curves in particular places requires slow and leak currents that vary appropriately on the slow time scale. In relating the behavior of two different models with the same fast components, comparison of the plots of the confining regions of the two sets of slow currents helps determine whether the models have similar bursting behavior. Of course, the location of the confining region is just a start, since where the trajectory goes inside the confining region depends on the specific dynamics of the slow currents.

Acknowledgments

This work was partially supported by the National Science Foundation and the Department of Energy.

References

1. E. Benoit, J. L. Callot, F. Diener, and M. Diener. Chasse au canards. *Collect. Math.*, 31:37–119, 1981.
2. N.M. Berezetskaya, V.N. Kharkyanen, and N.I. Kononenko. Mathematical model of pacemaker activity in bursting neurons of snail, *helix pomatia*. *J. Theor. Biol.*, 183:207–218, 1996.
3. R. Bertram, M. Butte, T. Kiemel and A. Sherman. Topological and phenomenological classification of bursting oscillations. *Bull. Math. Biol.* 57(3):413–39, 1995.
4. R.J. Butera Jr, J.W. Clark, C.C. Canavier, D.A. Baxter, and J.H. Byrne. Analysis of the effects of modulatory agents on a modeled bursting neuron:

- Dynamic interactions between voltage and calcium dependent systems. *J. Comp. Neurosci.*, 2:19–44, 1995.
5. R. J. Butera Jr, J. Rinzel and J. C. Smith. Models of respiratory rhythm generation in the pre-Bötzinger complex. I. Bursting pacemaker neurons. *J Neurophysiol.* 82:382–97, 1999.
 6. G.S. Cymbalyuk and R.L. Calabrese. Oscillatory behaviors in pharmacologically isolated heart interneurons from the medicinal leech. *Neurocomput.*, 32–33:97–104, 2000.
 7. G.S. Cymbalyuk and R.L. Calabrese. A model of slow plateau-like oscillations based upon the fast Na^+ current in a window mode. *Neurocomput.*, 38–40:159–166, 2001.
 8. G.S. Cymbalyuk, Q. Gaudry, M.A. Masino, and R.L. Calabrese. Bursting in leech heart interneurons: Cell-autonomous and network-based mechanisms. *J. Neurosci.*, 22:10580–10592, 2002.
 9. F. Dumortier and R. Roussarie Canard cycles and center manifolds *Mem. Amer. Math. Soc.* 121, no. 577, 1996.
 10. W. Eckhaus. Relaxation oscillations, including a standard chase on french ducks. *Lecture Notes in Mathematics*, 985:449–494, 1983.
 11. R. Fitzhugh. Impulses and physiological states in theoretical models of nerve membrane. *Biophys. J.*, 1:445–466, 1961.
 12. J.-M. Gambaudo, P. Glendinning and C. Tresser. The gluing bifurcation I: symbolic dynamics of the closed curves. *Nonlinearity* 1:203–214, 1988.
 13. J. Guckenheimer, S. Gueron, and R.M. Harris-Warrick. Mapping the dynamics of a bursting neuron. *Phil. Trans. R. Soc. Lond. B*, 341:345–359, 1993.
 14. J. Guckenheimer and P. J. Holmes. *Nonlinear Oscillations, Dynamical Systems, and Bifurcations of Vector Fields*. Springer-Verlag, New York, 1983.
 15. J. Guckenheimer and R. Oliva, Chaos in the Hodgkin-Huxley Model, *SIAM J. Appl. Dyn. Systems*, 1, 105–114, 2002.
 16. A.A.V. Hill, J. Lu, M.A. Masino, O.H. Olsen, and R.L. Calabrese. A model of a segmental oscillator in the leech heartbeat neuronal network. *J. Comput. Neurosci.*, 10:281–302, 2001.
 17. B. Hille, *Ionic Channels of Excitable Membranes, 3rd edition* Sinauer, 2001.
 18. Hodgkin, A. L. and Huxley, A. F. A quantitative description of membrane current and its applications to conduction and excitation in nerve, *J. Physiol. (Lond.)*, 116:500–544, 1952.
 19. E.M. Izhikevich. Neural excitability, spiking and bursting. *Internat. J. Bifur. Chaos Appl. Sci. Engrg.*, 10:1171–1266, 2000.
 20. C. Jones, Geometric singular perturbation theory. *Lecture Notes in Math.*, Springer, Berlin, 1609:44–118,1995
 21. R.H. Kramer and R.S. Zucker. Calcium-dependent inward current in *aplysia* bursting pace-maker neurones. *J. Physiol.*, 362:107–130, 1985.
 22. F. Nadim, O.H. Olsen, E. DeSchutter, and R.L. Calabrese. Modeling the leech heartbeat elemental oscillator: I. Interactions of intrinsic and synaptic currents. *J. Comput. Neurosci.*, 2:215–235, 1995.
 23. O.H. Olsen, F. Nadim, and R.L. Calabrese. Modeling the leech heartbeat elemental oscillator: II. Exploring the parameter space. *J. Comput. Neurosci.*,

- 2:237–257, 1995.
24. R.E. Plant. Bifurcation and resonance in a mathematical model for bursting nerve cells. *J. Math. Biol.*, 11:15–32, 1981.
 25. Rinzel, J. A formal classification of bursting mechanisms in excitable systems. Mathematical topics in population biology, morphogenesis and neurosciences (Kyoto, 1985), *Lecture Notes in Biomath.*, 71:267–281, Springer, Berlin, 1987.
 26. J. Rinzel and B. Ermentrout. Analysis of neural excitability and oscillations, in *Methods of Neural Modeling : From Synapses to Networks*, C. Koch and I. Segev, eds., MIT Press, 135–169, 1989.
 27. J. Rinzel and Y.S. Lee. Dissection of a model for neuronal parabolic bursting. *J. Math. Biol.*, 25:653–675, 1987.
 28. R. Roussarie. Bifurcation of planar vector fields and Hilbert’s sixteenth problem. *Progress in Mathematics*, 164. Birkhuser Verlag, Basel, 1998. xviii+204 pp.
 29. X.J. Wang. Multiple dynamical modes of thalamic relay neurons: Rhythmic bursting and intermittent phase-locking. *Neurosci.*, 59:21–31, 1994.